ANTIOXIDANTS & REDOX SIGNALING
Volume 9, Number 4, 2007

DOI: 10.1089/ars.2006.1296

Original Research Communication

Spatial Coordination of Cell-Adhesion Molecules and Redox Cycling of Iron in the Microvascular Inflammatory Response to Pulmonary Injury

NIKOLAI V. GORBUNOV,[1] DIPAK K. DAS,[2] SHYAMAL K. GOSWAMI,[2] NARASIMMAN GURUSAMY,[2] and JAMES L. ATKINS[1]

ABSTRACT

Transmigration of phagocytic leukocytes (PLCs) from the peripheral blood into injured lung requires a conversion of the microvascular endothelial cells (ECs) to the proinflammatory phenotypes and spatiotemporal interplay of different types of cell adhesion molecules (CAMs) on PLC and endothelium. The present report is focused on involvement of iron-dependent redox signaling in spatial coordination of lung CAM due to either a pulmonary trauma or endotracheal iron administration in rats. Redox alterations, deposition of 3-nitrotyrosine, expression of VE-cadherin, ICAM-1, and the PLC integrins, and the status of thioredoxin, Ref-1, NF-κB and Nrf2 redox-sensitive elements in the alveolar microvasculature were assessed with EPR spectroscopy, immunobloting, and confocal microscopy. We demonstrated for the first time *in vivo* that the presence of catalytically active iron, deposition of myeloperoxidase, and induction of the oxidative stress in the lung-injury models were accompanied by (a) downregulation of VE-cadherin, (b) upregulation and polarization of ICAM-1 and the PLC integrins, and (c) nuclear translocation and interaction of thioredoxin, Ref-1, and NF-κB and complex structural changes in EC and PLC at the sites of their contacts. The studies suggested that a part of the proinflammatory action of iron in the lung resulted from its stimulation of the redox-sensitive factors. *Antioxid. Redox Signal.* 9, 483–495.

INTRODUCTION

The inflammatory response to lung trauma is characterized by the emigration of blood-borne phagocytic leukocytes (PLCs) [*i.e.*, polymorphonuclear neutrophils (PMNs) and monocytes] across the microvascular wall into the alveolar lumen (10, 28, 31, 33). Transendothelial migration (TEM) (*i.e.*, diapedesis) of PLCs in the lung capillary bed is a multistage process that involves spatial coordination and interaction of a number of cell-adhesion molecules (CAMs) on the microvascular endothelium (EC) and PLCs (5, 10, 26, 31, 33, 34). Although there has been intense study of systemic mediators that activate PLCs and attract them to the inflammatory site, less is known about the local process that coordinates the changes in the PLCs and EC, or the three-dimensional aspects of this coordination, which can be assessed only in an intact lung.

It was demonstrated recently that release of iron from ruptured cells and PLC activation cause the traumatic oxidative stress (OS) that eventually contributes to the complex proinflammatory alterations (6, 12). Moreover, the presence of high levels of pro-oxidant labile iron and reactive oxygen species has been shown *in vitro* to upregulate the PLC/EC adhesion and the expression of the ICAM-1 adhesion molecules on EC, suggesting that the redox signaling can coordinate PLC chemotaxis and the microvascular inflammatory response (8, 18, 19). Several universal cascade mechanisms exist, including Rac-11/NF-κB, for transduction and propa-

[1]Walter Reed Army Institute of Research, Silver Spring, Maryland.
[2]Cardiovascular Research Center, University of Connecticut School of Medicine, Farmington, Connecticut.

gation of redox signals, which could potentially coordinate responses in both PLCs and EC through upregulation of CAMs (6, 8, 19, 21, 30). However, involvement of the labile iron in PLC TEM and its potential role in these proinflammatory events in lung trauma remains speculative and has not been previously examined *in vivo* (2, 27, 32).

Using a model of hemorrhagic pulmonary contusion, we demonstrated recently that the lung trauma is associated with recruitment and extravasation of the inflammatory PLCs, accumulation of extracellular myeloperoxidase (MPO), development of nitroxidative stress to EC, and upregulation of antioxidant proteins such as superoxide dismutase (SOD-II) and heme oxygenase (HO-1) that occur in time-dependent manner (13).

The aim of the present study was (a) to examine changes in expression and localization of adhesion molecules in the EC and PLCs in the lung to assess their 3D spatial coordination, and (b) to determine whether this remodeling of the lung microvascular CAM assemblies is associated with redox responses in both hemorrhagic lung trauma and the intratracheal instillation of iron nitriloacetate.

MATERIALS AND METHODS

Animal models

Pathogen-free male Sprague–Dawley rats (~280 g body weight; Charles River Laboratories Inc., Wilmington, MA) were housed in individual cages in climate-controlled animal quarters and were given water and food *ad libitum*.

Lung trauma was produced in animals by exposure to a shock wave. After acclimatization, rats were randomly assigned to the "SW exposure," "sham to SW exposure," "iron administration," and "sham to iron administration" groups. All animals were anesthetized with ketamine (60 mg/kg of body weight, IP). Animals from the "SW exposure" group were subjected to lung trauma by impact of SW. The compressed air–driven shock tube generated a single SW with main harmonic frequency at 260 ± 5 Hz and peak overpressure at 118 ± 7 kPa (at peak overpressure). The pressure–time history of the SW was recorded at each exposure. Previous experiments demonstrated that SWs at this level of overpressure produced the most consistent lung injury (12). Twenty rats exposed to SWs were subjected to lung tissue samplings at 3, 6, 12, and 24 h after exposure. Tracheotomy followed by endotracheal pulse administration of iron (Fe^{2+}) in complexes with either nitriloacetate ($NTA_2Fe_3^{2+}$) or *N,N′*-bis (2-hydroxybenzyl) ethylenediamine-*N,N*′-diacetic acid (HBED), a polyphenolic iron chelator with antioxidant properties (3, 26) (15 μmol/kg), was conducted with 10 animals. Five anesthetized animals were assigned to treatment with 0.2 ml of saline solution vehicle (USP grade) (sham-treated group). Samples of lung and the peripheral blood were assessed with gross pathology, histology, low-temperature EPR spectroscopy, immunoblotting, and immunofluorescence image analyses, for the status of (a) ICAM-1, α_M- and β_2-integrins, and VE-cadherin adhesion molecules; (b) iron-containing complexes, free radical species, MPO, and 3-nitrotyrosine (3NTyr); and (c) thioredoxin (TRX), redox factor-1 (Ref-1/APE-1), nuclear factor κB (NF-κB p50 and p65), and nuclear factor E2–related factor 2 (Keap1/Nrf2) redox-sensitive elements.

Animal handling and treatments were conducted in compliance with the Animal Welfare Act and other Federal statutes and regulations related to animals, and experiments involving animals adhered to principles stated in the Guide to the Care and Use of Laboratory Animals, National Research Council. The facilities are fully accredited by the Association for Assessment and Accreditation of Laboratory Animal Care International.

EPR techniques

Low-temperature EPR spectroscopy of lung and blood samples was conducted as described previously (12). In brief, the samples placed in 1-ml syringes (Henke-Sass, Wolf; Gmbh, Germany) were frozen immediately in liquid nitrogen to make them of constant volume and geometric profile. Low-temperature EPR spectra were recorded with X-band EMX EPR spectrometer (Bruker Instruments, Inc., Hamburg, Germany). The recorded EPR spectra were integrated using the WINEPR program package (Bruker Instruments).

Lung tissue preparation for histology and immunofluorescence microscopy

Lung tissue samples were collected at necropsy, fixed in 4% buffered paraformaldehyde (pH 7.4), embedded and frozen in O.C.T. compound, and subjected to cryosectioning. The obtained specimens (7-μm sections) were stained with hematoxylin and eosin for histologic examinations or processed for the fluorescence confocal microscopy.

Staining for nonheme iron complexes

Lung tissue was stained with Mallory's reagent for iron to reveal a spatial localization of the iron complexes in the alveolar cells. The specimens were analyzed with an Olympus AX 80 microscope equipped with objective lenses (x40 and x100). Optical images were recorded with DP 70 color digital camera.

Immunoblot analysis

Alterations in the amount of ICAM-1 in lung hemorrhagic lesions were assessed using immunoblot techniques followed by protein separation in polyacrylamide gels. For this purpose, frozen sections of hemorrhagic foci and identical lung sites from sham-treated animals were disintegrated under liquid nitrogen and subjected to lysis in a buffer containing 10 m*M* EDTA, 150 m*M* NaCl, 50 m*M* Tris HCl (pH 7.5), 1% Triton X-100, 0.1% SDS, and a mixture of protease inhibitors (5 μg/ml aprotinin, 10 μ*M* leupeptin, 2 m*M* EDTA, and 1 m*M* phenylmethylsulfonyl fluoride). The further protein separations and immunobloting were conducted as described previously (13). The primary antibodies used for hybridization were: mouse anti-ICAM-1 IgG (Santa Cruz Biotechnology, Inc., Santa Cruz, CA; www.scbt.com).

For assessment of nuclear and cytosol fractions of NF-κB p65 and nuclear interaction of NF-κB p65 with Ref-1 tissue homogenates were centrifuged at 3,000 rpm at 4°C for 15

min, and the supernatant was used as the cytosol extract. The nuclear pellet was resuspended in five volumes of buffer that was essentially the same, except containing 500 m*M* NaCl. The nuclei were lysed by incubation for 1 h on ice with intermittent tapping. Homogenates were then centrifuged at 10,000 rpm at 4°C for 15 min, and the supernatant was used as nuclear lysate. Protein concentration was determined using BCA Protein Assay Kit (Pierce, Rockford, IL).

To reveal NF-κB p65 complexes with Ref-1, nuclear extracts containing 500 μg of total protein were immunoprecipitated with anti-NF-κB p65 subunit monoclonal antibody (sc-8008; Santa Cruz Biotechnology, Santa Cruz, CA), and Protein A Sepharose beads (Zymed, San Francisco, CA) at 4°C overnight. Pellets were collected by centrifuging at 10,000 *g* for 30 s at 4°C, and were washed 3 times with ice-cold buffer (50 m*M* Tris-HCl, pH 7.4, 150 m*M* NaCl, 1% NP-40, 0.5% sodium deoxycholate, 0.1% SDS, and 2 m*M* EDTA). Pellets were resuspended in 1× Laemmli sample buffer and boiled for 10 min. Proteins were separated in SDS-PAGE (10%) and transferred to nitrocellulose filters. Filters were blocked in 5% nonfat dry milk and probed with anti-Ref-1 rabbit polyclonal antibody (sc-334; Santa Cruz Biotechnology). Protein bands were identified with horseradish peroxidase–conjugated secondary antibody and Western blotting Luminol Reagent (Santa Cruz Biotechnology).

Semiquantitative assessment of immunoblots was conducted using ImageJ image processing software (http://rsb.info.nih.gov).

Immunofluorescence techniques and image analysis

The obtained lung specimens (see earlier) were processed for the immunofluorescence imaging, as described previously (13). In brief, the tissue sections were washed with PBS, incubated in PBS containing 2% paraformaldehyde and 0.1% Triton X-100 for 20 min, washed 3 times with PBS, and then once with PBS containing 0.5% BSA and 0.15% glycine (buffer A). Any nonspecific binding was blocked by incubating the samples with purified goat and/or donkey, and/or rabbit normal serum (Santa Cruz Biotechnology) diluted 1:20 in buffer A. The primary antibody against (a) VE-cadherin (goat polyclonal IgG from Santa Cruz Biotechnology); (b) ICAM-1 (rabbit polyclonal IgG from Santa Cruz Biotechnology); (c) thioredoxin (goat polyclonal IgG, Santa Cruz Biotechnology); (d) Ref-1 (mouse monoclonal IgG, Santa Cruz Biotechnology); (e) Nrf2 (goat polyclonal IgG, Santa Cruz Biotechnology); (f) myeloperoxidase and NF-κB p50 (rabbit polyclonal IgG from Calbiochem, San Diego, CA); (g) α_M-integrins (mouse monoclonal IgA) and β_2-integrins (mouse monoclonal IgG) (from BD PharMingen, San Diego, CA; www.bdbiosciences.com); (h) anti-3-nitrotyrosine (mouse polyclonal IgG from Calbiochem); and (i) PECAM-1 (goat polyclonal IgG, Santa Cruz Biotechnology) were used in 1:250 dilution in buffer A. This was followed by three additional washes with buffer A and incubation with secondary fluorochrome-conjugated antibody and/or streptavidin-AlexaFluor 594 conjugate (Molecular Probes, Inc., Eugene OR), and with Hoechst 33342 (Molecular Probes) diluted 1:5,000.

The secondary antibodies used were (a) ALEXA 488 conjugated rabbit anti-goat IgG, ALEXA 594 conjugated donkey anti-goat IgG, ALEXA 594 conjugated chicken anti-rabbit IgG, and ALEXA 594 conjugated chicken anti-mouse IgG (Molecular Probes); and (b) Cy2 conjugated goat anti-rabbit IgG, and Cy3 conjugated donkey anti-mouse IgG (Rockland Inc., Gilbertsville, PA). Negative controls for nonspecific binding included (a) normal rabbit serum without primary antibody, or (b) with secondary antibody alone, or (c) IgA isotype-biotin antibody for α_M-integrins, markers of PLC, as described previously (12). The specificity of binding of anti-3NTyr antibody was tested as described previously (13). Assessment of colocalization of immunoreactivity of ICAM-1 with PECAM-1, a marker of vascular endothelial cells, was used to identify the cell-specific expression of ICAM-1 in the injured lung. The specimens were analyzed with an Olympus AX 80 microscope equipped with a Hamamatzu digital camera and with a Bio-Rad Radiance 2100 confocal microscope system. Processing and analysis of digital images were conducted using SimplePCI High Performance Imaging software (Compix Inc., www.cimaging.net) and ImageJ software (http://rsb.info.nih.gov).

Statistical analysis

Data are expressed as individual data points or means ± SEM. Differences were evaluated using one-way analysis of variance (ANOVA) with Tukey's *post hoc* multiple comparisons test. Differences were considered significant at $p < 0.05$.

RESULTS

Iron redox cycling and redox signaling in the models of lung injury

We used a two-model system to investigate association of iron-induced OS with proinflammatory alterations in lung. In the first model, the lung injury was produced by exposure of animals to SW, which caused alveolar septa rupture, blood extravasation, and alveolar influx of heme and nonheme ferrous complexes along with the plasma ferric transferrin (Fig. 1A and B). In the second model, the inflammation was produced by endotracheal administration of ferrous complexes [iron/nitrilotriacetate ($NTA_2Fe_3^{2+}$) or $NTA_2Fe_3^{2+}$ with HBED, a chelator and antioxidant, in saline solution] (Fig. 1C–E). Both interventions led to increased transferrin-bound ferric iron in the blood within 40-min post-treatments that was prevented by administration of HBED (not shown). Thus, at this time, the amounts of the transferring-bound iron in the peripheral blood of the SW-exposed and $NTA_2Fe_3^{2+}$-treated groups were 32.7 ± 4.8 and 43.4 ± 5.1 μ*M*, respectively (*vs*. sham to iron-administration group, 21.1 ± 2.7 μ*M*). Cellular uptake of iron could occur through the transferrin receptor–mediated endocytosis (for Fe^{3+}) and/or via the divalent metal transporter (DMT1/Nramp2) (for Fe^{2+}). Although the Nramp2 upregulation occurred in these models (not shown), whether an increase in the intracellular iron occurred remained unclear. Therefore, we assessed intercellular iron using histochemical analysis staining with Mallory's reagent.

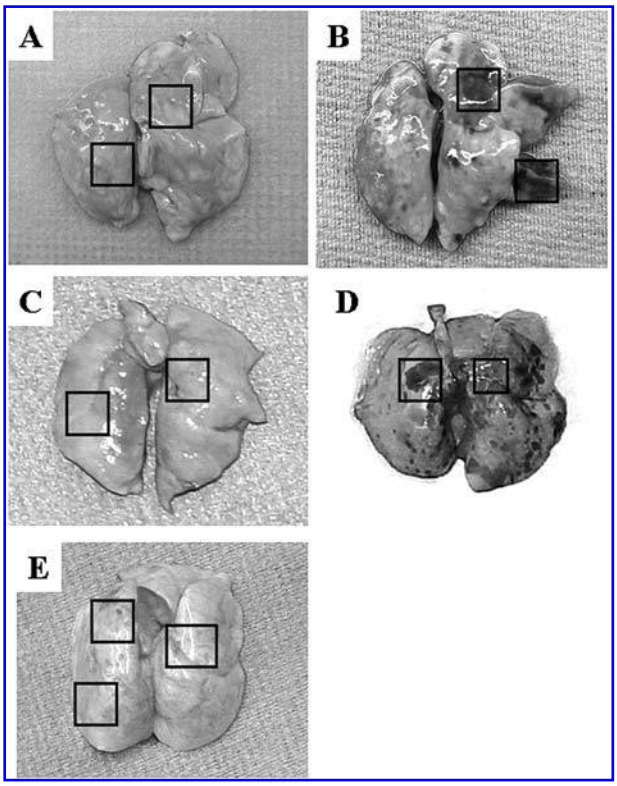

FIG. 1. Gross pathology of lung at 3 h after exposure to shock-wave (SW) or iron administration. (**A**) Sham to SW exposure. (**B**) SW exposure. (**C**) Sham to iron administration. (**D**) Iron administration. (**E**) Iron administration with HBED chelator. Injured areas subjected to analyses are indicated by black squares.

A distinguishable deposition of Fe^{3+} was noted in the alveolar cells of the injured lung and the lung exposed to $NTA_2Fe_3^{2+}$ (Fig. 2A–D). The results of histochemistry were confirmed by low-temperature EPR spectroscopy: a substantial increase in the signals at g~4.3 corresponding to the nontransferrin high-spin Fe^{3+} complexes in hexagonal symmetry (distinguishable from the EPR signals of the plasma transferrin bound iron), was observed in the presence of the iron-positive staining (see Fig. 1E). At that stage, the EPR-detectable amounts of nontransferrin high-spin Fe^{3+} complexes in the lung of SW-exposed and $NTA_2Fe_3^{2+}$-treated animals were 2.3 ± 0.5 and 8.2 ± 1.4 μ*M*, respectively, whereas these parameters in sham-treated groups were at the level of EPR sensitivity *(i.e.*, <0.3 μ*M*) ($p < 0.01$; $n = 5$). These effects were accompanied by an increase in the EPR signals of free radical signals ($g = 2.008$) in the lung of treated animals (*vs*. sham). A typical increment free radical signal calculated from a representative EPR signal of SW-treated and $NTA_2Fe_3^{2+}$ -treated lung is shown in Fig. 2F. This increase was 70–120% in the SW-exposed group and >200% in the $NTA_2Fe_3^{2+}$-exposed group. A compensatory response to the microcirculatory insult in lung was accompanied by systemic hypotension and release in lung nitric oxide (NO) detected with the EPR spin-trapping techniques (14). Thus, the amount of HbNO in the peripheral blood at 3-h observations was 2.4 ± 0.3 μ*M* (SW exposure) and 1.9 ± 0.2 μ*M* ($NTA_2Fe_3^{2+}$ administration), whereas in sham-treated animals, this parameter did not exceed 0.8 ± 0.2 μ*M* ($p < 0.01$, $n = 5$).

The resulting iron-induced OS to lung downregulated the redox-sensitive VE-cadherin adhesion junctions (Fig. 3), which are the major "keepers" of endothelial integrity of microvasculature in the alveolar septa (10, 32). Indeed, a substantial decrease in the expression of VE-cadherin correlated with the formation of 3NTyr (a product of oxidative injury) in the cell membrane proteins [Pearson $r = 0.39$ for interference of signals from green (VE-cadherin) and red (3NTyr) channels, a specimen example from SW-injury] and deposition of the PLC-released MPO, which were identified recently as "footprints" of PLCs in the extracellular matrix and a promoter of OS (20, 21).

Oxidative stress induces a number of adaptive cell responses driven by redox signaling cascades. We further investigated whether redox-sensitive elements known to be mediators of redox signaling of the inflammatory response (*i.e.*, thioredoxin (TRX), NF-κB, Ref-1, and Nrf2) were affected in our lung-injury models. The redox-dependent induction of these factors is shown to be associated with their nuclear translocation. Moreover, evidently nuclear translocation of TRX and Ref-1 and the TRX-dependent reduction of Ref-1 in the nuclear sphere are prerequisites for transcriptional activity of NF-κB (15, 17, 22). Thus, we expected that iron redox cycling and associated OS in lung would cause a detectable spatial interaction of TRX/Ref-1 and Ref-1/NF-κB in the cell nuclei. To demonstrate nuclear translocation of these redox-sensitive elements, we analyzed lung specimens with immunofluorescence confocal microscopy and immunoblotting techniques.

Representative fluorescence images (XY projections taken with 0.5-μm Z-steps) of TRX (green channel) and Ref-1 (red channel) with nuclear counterstaining (blue channel) obtained from lung specimens are shown in Fig. 4A–C. Presumably, the spatial interaction of TRX and Ref-1 in nuclei should appear in the projections of the confocal optical sections as gradual change of nuclear color from blue to light yellow and white because of interference of red (Ref-1), green (TRX), and blue (nucleus) lights. As shown in Fig. 4B and C, this effect was observed in the specimens obtained from the injured lung (SW and $NTA_2Fe_3^{2+}$ treatments) but not in "sham to SW exposure" (not shown) and "sham to iron administration" groups of animals (Fig. 4A). A montage presented in the panel 4E is the computer-reconstructed XZ projections (0.5-μm Y steps for the image stack reslicing) of TRX, Ref-1, and nucleus of the selected area in the panel 4C. The images presented in the panel 4E demonstrate Z extent of 3-D nuclear colocalization of TRX and Ref-1 (white color interference).

Interestingly, nuclear localization TRX in the injured lung was frequently higher in the sites of increased expression of ICAM-1 adhesion molecules on the vascular endothelium (Fig. 4D and reconstructed montage 4F) that let us further speculate on association of redox and ICAM-1 responses in the lung microvascular endothelium in our models.

The increase in nuclear levels of TRX and Ref-1 could result in TRX-dependent reduction and activation of the nuclear fraction of Ref-1, which is essential for molecular interaction with NF-κB and induction of NF-κB–dependent transcription (16, 17, 25).

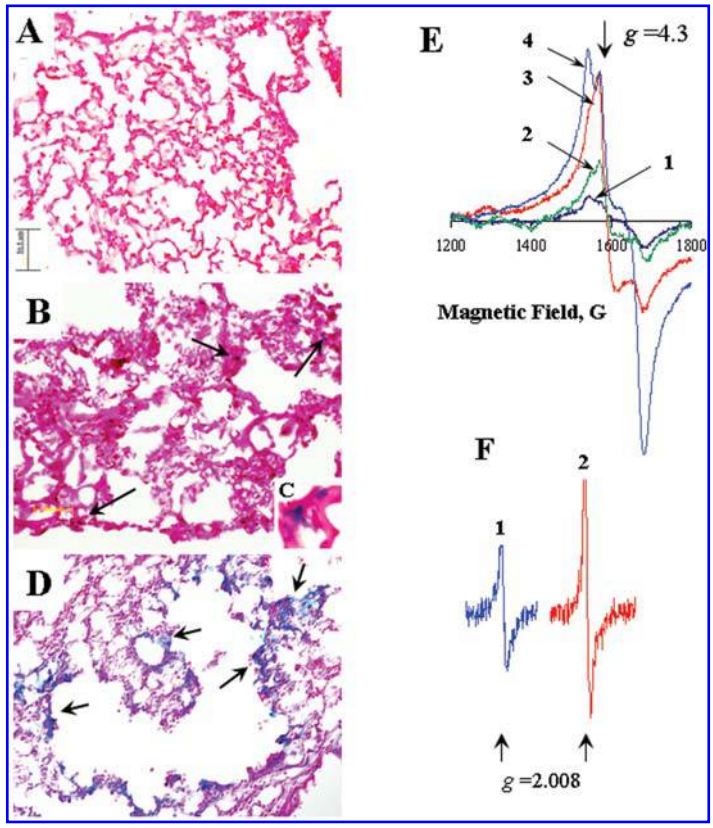

FIG. 2. Assessments of the iron redox transformations and deposition of heme-free (labile) ferric iron in the lung specimens obtained from animals exposed to shock wave or treated with ferrous iron complexes. (**A**–**D**) Representative images of the histochemical staining of lung sections from sham-treated (**A**, 40x image magnification) ("sham to iron administration" group), SW-exposed (**B**, 40x image magnification), and $NTA_2Fe_3^{2+}$-treated (**D**, 40x image magnification) animals for ferric iron with the Mellory reagent. Inset (**C**) is 5x zoom of a selected area in (**B**). Deposition of ferric iron in lung cells (in blue) is indicated with green arrows. Note bars are 50 μm. (**E**) Representative low-temperature EPR spectra of the nonheme ferric complexes in the lung of sham-treated [*i.e.*, sham to $NTA_2Fe_3^2$ administration (1), SW-exposure (2), and $NTA_2Fe_3^{2+}$-treated animals (3)]. Increase of the EPR signal at $g = 4.3$ observed in "SW-exposure" and "$NTA_2Fe_3^{2+}$-treatment" groups at 3 h after treatment. For comparison, see spectrum (4) of blood plasma sample containing 35 μ*M* iron–transferrin complexes. (**F**) Representative increments of the low-temperature EPR signal of the free radical species in the SW-exposed (1) and $NTA_2Fe_3^{2+}$-treated (2) lung (*vs.* a signal from the respective sham-treatment groups).

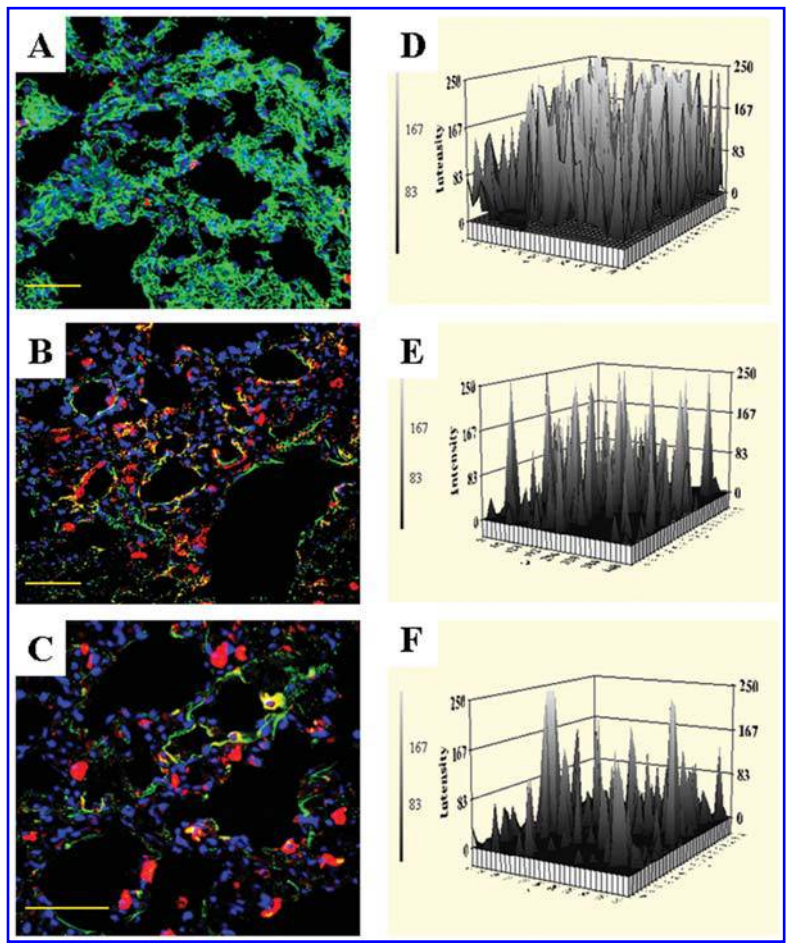

FIG. 3. Alterations in the expression of VE-cadherin and accumulation of 3-nitrotyrosine (3-NTyr) in the lung specimens from the animals subjected to shock-wave (SW) exposure or $NTA_2Fe_3^{2+}$ treatment. (**A**–**C**) Representative projections of VE-cadherin (green channel, Alexa 488) and 3-NTyr (C, red channel, Cy3) in the lung specimens from sham-treated (sham to SW exposure) (**A**); SW-exposed (**B**) and $NTA_2Fe_3^{2+}$-treated (**C**) animals. The relative immunofluorescence of VE-cadherin is presented respectively in (**D**–**F**). A relative decrease in the immunofluorescence of the expressed VE-cadherin was observed in (**E**) and (**F**) (compare with **D**) at 3 h after treatments. Counterstaining of nuclei was with Hoechst 33342; yellow color results from the interference of the green and red projections in the presented images. Bars are 50 μm. All images are representative of analyses conducted by using five animals.

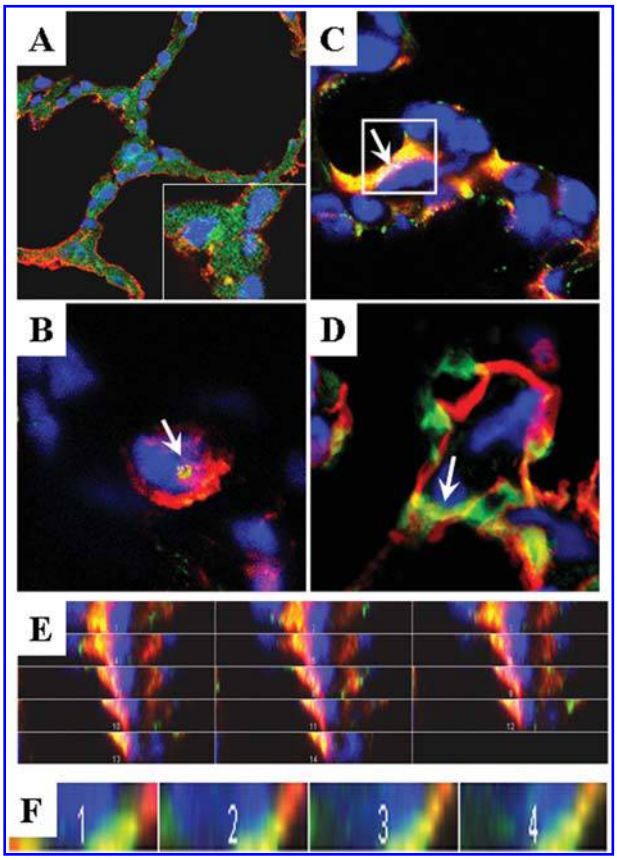

FIG. 4. Assessment of nuclear colocalization of Ref-1 and Thioredoxin (TRX) in the lung specimens from the animals subjected to shock-wave exposure or $NTA_2Fe_3^{2+}$ treatment (3 h after treatment). (**A–C**) Representative projections of Ref-1 (red channel, Alexa 594) and TRX (green channel, Alexa 488) in the lung specimens obtained from sham-treated (**A**, 100x magnification; "sham to iron administration" group), SW-exposed (**B**, 100x magnification, 4x zoom), and $NTA_2Fe_3^{2+}$-treated (**C**, 100x magnification, 4x zoom) animals. Counterstaining of nuclei with Hoechst 33342 appears in blue. Nuclear colocalization of Ref-1 and TRX appears as white foci from interference of red, green, and blue colors (indicated with arrows in **B** and **C**). Inset in (**A**) is a selected area magnified with zoom 4x. (**D**) A projection of the spatial localization of TRX (green channel) in an endothelial cell, which is defined by the ICAM-1 immunofluorescence (red channel), in a specimen of the SW-injured lung section (arrow). The counterstaining of a nucleus was with Hoechst 33342 (blue channel). Nuclear localization of TRX appears in turquoise. Magnification is 100x, zoom 4x. (**E**) A set of images obtained by 0.5-μm Y-reslicing of the stack of 10 Z projections of the indicated area (**C**), which demonstrates the nuclear colocalization of Ref-1 and TRX (in white). (**F**) A set of images obtained by 0.5-μm Y-reslicing of the stack of 10 Z projections of the indicated area in (**D**), which demonstrates the nuclear localization of TRX (in turquoise) in the cells with positive staining for ICAM-1 expression.

To assess nuclear interaction of Ref-1 and NF-κB, we applied confocal image-analysis techniques in combination with fractional immunoblotting and co-immunoprecipitation of Ref-1 with NF-κB. The presence of co-localization of immunoreactivity of NF-κB and Ref-1 in the nuclear sphere was determined in the lung sections from SW-exposed and $NTA_2Fe_3^{2+}$-treated lung (Fig. 5). As shown in Fig. 5B and C, this effect was observed in the specimens obtained from the injured lung (SW and $NTA_2Fe_3^{2+}$ treatments) but not in "sham to SW exposure" (Fig. 5A) and "sham to iron administration" groups of animals (not shown).

To demonstrate Z extent of spatial colocalization of Ref-1 and NF-κB in the nuclear sphere, we present a montage of images obtained by 0.5-μm Y-reslicing of the stack of 10 Z projections of the area indicated in the panel B (Fig. 5D). Nuclear colocalization of Ref-1 and NF-κB has appeared in white color in Fig. 5D as the result of interference of blue, green, and red colors. The results of semiquantitative analysis of immunofluorescence of NF-κB in the selected areas of the

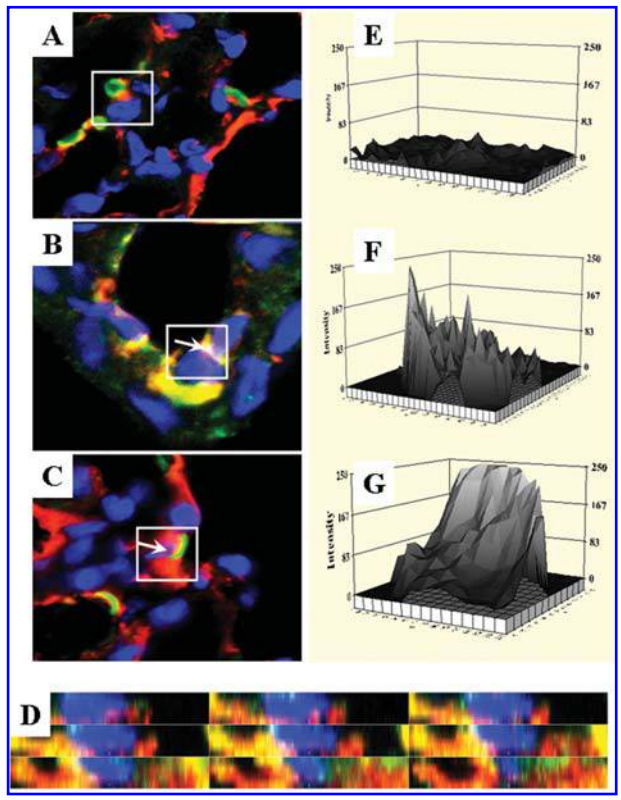

FIG. 5. Assessment of nuclear colocalization of Ref-1 and NF-κB p50 in the lung specimens from the animals subjected to shock-wave exposure or $NTA_2Fe_3^{2+}$ treatment (3 h after treatment). (**A–C**) Representative projections of Ref-1 (red channel, Alexa 594) and NF-κB p50 (green channel, Cy2) in the lung specimens obtained from sham-treated (**A**, 100x magnification, 2x zoom) ("sham to SW exposure" group), SW-exposed (**B**, 100x magnification, 4x zoom), and $NTA_2Fe_3^{2+}$-treated (**C**, 100x magnification, 4x zoom) animals. Counterstaining of nuclei was with Hoechst 33342. Nuclear colocalization of Ref-1 and NF-κB p50 appears as white foci from interference of red, green, and blue colors (arrows in **B** and **C**). (**D**) A set of images obtained by 0.5-μm Y reslicing of the stack of 10 Z projections of the area indicated in (**B**), which demonstrates the nuclear colocalization of Ref-1 and NF-κB p50 (white). (**E–G**) Distribution of relative immunofluorescence of NF-κB p50 in the selected nuclear areas (white squares) of the respective images: (**A**) sham treatment), (**B**) SW exposure, and (**C**) iron administration.

obtained images 5A–C are presented in the panels 5E–G. Increase in the relative intensity of this parameter in "SW exposure" and "iron-administration" groups indicates induction of nuclear translocation of NF-κB. The data obtained with confocal immunofluorescence analysis were confirmed using immunoblotting techniques. As shown in Fig. 6A and B, SW exposure resulted in a significant increase in the nuclear fraction of NF-κB p65 and a decrease in the cytoplasmic fraction in the injured foci (in comparison with respective sham treatment). This effect was simulated by administration of $NTA_2Fe_3^{2+}$, an activator of OS (see Fig. 6C). The effect of $NTA_2Fe_3^{2+}$ was substantially eliminated by HBED, a polyphenolic chelator of iron, which also suppressed formation of free radical species (see Fig. 6). Moreover, we found that HBED reduced deposition of the catalytically active iron in plasma transferrin and facilitated excretion of iron in urine in both models of injury (not shown).

Immunoprecipitation of the nuclear fractions of NF-κB p65 with a subsequent immunoblotting of the precipitated proteins for Ref-1 protein revealed the presence increase in the amounts of Ref-1/NF-κB complexes in the fractions of injured lung (Fig. 6F). We suggest that OS in the investigated models of lung injury increased the nuclear translocation of TRX and Ref-1 that apparently resulted in augmentation of the nuclear formation of Ref-1/NF-κB complexes.

Representative projections of Nrf2 (green channel, Alexa 488) in the lung specimens obtained from sham-treated ("sham to iron administration" group), SW-exposed, and $NTA_2Fe_3^{2+}$-treated animals is presented in Fig. 7A–C. Because we did not see any differences between "sham to SW exposure" and "sham to iron administration" groups in respect to Nrf2 response, we reported in panel 7A an image from "sham to iron administration" group. To demonstrate Z extent of nuclear translocation of Nrf2, we have presented a montage of images obtained by 0.5-μm Y-reslicing of the stack of 10 Z projections of the area indicated in panel C (Fig. 7). Nuclear localization of Nrf2 appears in turquoise color in Fig. 7D as the result of interference of blue and green colors. The increase in nuclear localization of Nrf2 demonstrated with immunofluorescence imaging was confirmed with immunoblotting of Nrf2 in the nuclear subcellular fraction (not shown).

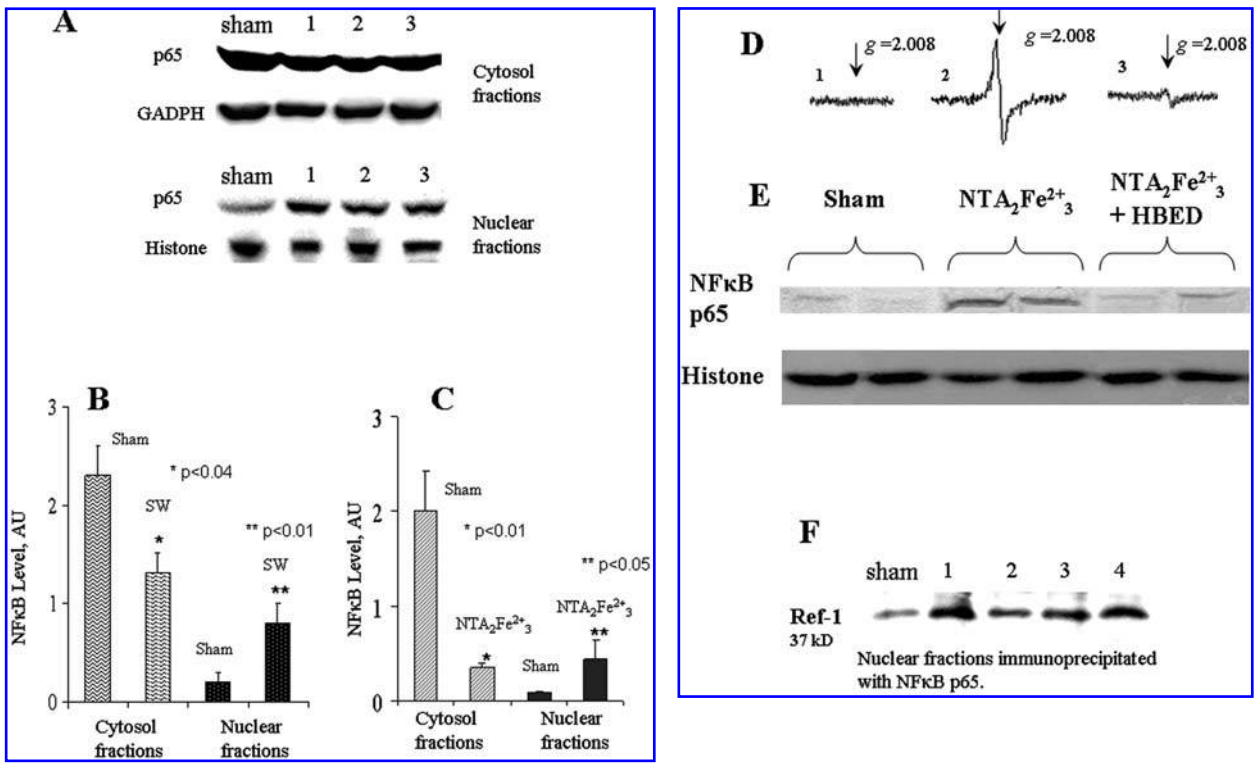

FIG. 6. Immunoblot analysis of NF-κB p65 distribution between cytosol and nuclear fractions in the lung specimens from the animals subjected to shock-wave exposure or $NTA_2Fe_3^{2+}$ treatment (3 h after treatment): assessment of nuclear interaction of NF-κB and Ref-1 nuclear factors. (**A**) Representative immunoblot of NF-κB p65 in the lung specimens from SW-induced injury (in triplicate: 1–3, *vs*. respective sham treatment). (**B, C**) Assessment of alterations in the fractional distribution of NF-κB p65 induced by SW exposure (**B**) and iron administration (**C**). (**B**) $^{*}p < 0.04$ (SW *vs.* respective sham treatment, Tukey's test); $^{**}p < 0.01$ ($NTA_2Fe_3^{2+}$ treatment *vs*. sham treatment, Tukey's test). (**C**) $^{*}p < 0.01$ (SW *vs.* respective sham treatment, Tukey's test); $^{**}p < 0.05$ ($NTA_2Fe_3^{2+}$ treatment *vs*. sham treatment, Tukey's test). (**D**) Effect of HBED chelator on induction of free radicals due to administration of $NTA_2Fe_3^{2+}$; representative increments of free radical signals obtained from sham to $NTA_2Fe_3^{2+}$ administration group (1), $NTA_2Fe_3^{2+}$ administration group (2), and $NTA_2Fe_3^{2+}$ administration with HBED group (3). (**E**) Effect of $NTA_2Fe_3^{2+}$ and HBED chelator on nuclear levels of NF-κB p65; immunoblot data are presented in duplicate. (**F**) Assessment of augmentation of interaction of the nuclear fractions of NF-κB and Ref-1 due to lung injury: 1–2, SW exposure; 3–4, iron administration (compare with sham to SW exposure).

Overall, the data presented in Figs. 4 through 7 indicated that oxidative stress produced by either hemorrhagic lung injury or deposition of iron in lung led to activation of transcriptional factors containing thiol redox-sensors [(*i.e.*, NF-κB and Nrf2 (15–17, 23)]. This redox transcriptional response could drive adaptive inflammatory remodeling alterations in microvascular cells (30).

Inflammatory remodeling in lung microvasculature induced by shock-wave exposure and iron administration

Assessment of the markers presented in the preceding paragraph provides the evidence of OS in lung followed by the induced injury. It is well accepted that OS plays a crucial role in the induction of the proinflammatory cell adhesion molecules on PLC and parenchyma cells of a hosting tissue. Reactive oxygen and nitrogen species, such as hydrogen peroxide, superoxide anion radical, and peroxynitrite, are capable of activating constitutively present forms of ICAM-1 and promoting their transcriptional expression (8, 30, 37). Therefore, redox signaling has emerged recently as a mechanism for both early and long-term inflammatory transformations.

The images presented in Fig. 8A–C and the respective relative intensity of immunofluorescence estimated for ICAM-1 shown in Fig. 8E–G demonstrate that the lung injury due to SW exposure and $NTA_2Fe_3^{2+}$ was associated with both increase in the membrane immunoreactivity for ICAM-1 adhesion molecules and PLC sequestration and migration to the alveolar space within 3 h after exposure. This induction of ICAM-1 was inhibited in the presence HBED (Fig. 8D and H), which suggested association of the ICAM expression with iron-induced oxidative stress. This ICAM-1 expression was unlikely to be due to the *de novo* protein synthesis at 3 h after exposure, because we have not observed a significant increase of ICAM-1 protein in lung SW-treated animals at that time (0.56 ± 0.09 *vs.* 0.39 ± 0.06 A.U.; $p < 0.1$, Tukey's test). That increase occurred substantially later at 6 h after exposure and remained elevated through the 24-h observation (Fig. 8I). Therefore, we assumed that iron-dependent OS triggered remodeling of the microvascular EC CAM system and eventually mediated transformation of EC cells to the proinflammatory phenotype(s). This cascade of events developed in the alveolar microvasculature attracted blood PLC (Fig. 9). The induced alterations in the alveolar parenchyma cells along with the inflammatory cell repopulation resulted in the appearance of inflammatory foci (Fig. 9A), which we tentatively named "inflammatomes."

"Homing" of the phagocytic leukocytes and associated 3-D coordination of ICAM-1 in pulmonary microvessels during inflammatory response to trauma and iron-induced oxidative stress

Deposition of Fe and development of pulmonary "inflammatomes" were associated with upregulation of endothelial ICAM-1 and the PLC accumulation in the microvasculature (see Fig. 8).

Further to assess the TEM of PLC in the sites of inflammation, we applied immunofluorescence confocal imaging of PLC-specific β_2- and α_M-integrins, and MPO. Complexes of β_2-integrins with α_L- and α_M-integrins are known to form LFA-1 and MAC-1 receptor systems, which mediate TEM by interacting with their counter-receptors on EC *(i.e.*, ICAM-1 and VCAM-1) (4, 29). The presence of synchronous spatial coordination of PLC integrins with VCAM-1 and ICAM-1 was documented recently in the models of PLC interaction with EC monolayers (1, 4). In these dynamic events, MPO can react as both a component of the inflammatory response mechanism specific for the granulocytic PLC and an autocrine and paracrine stimulator of their MAC-1 receptor systems (20).

As shown in Fig. 9A and B, alterations in the chemotactic PLCs in the "inflammatomes" were characterized by the conversion from round to polarized morphology with the lamellipod-like projection of β_2- and α_M- integrins at the leading edge. Individual sensitized PLCs used lamellar cytoplasmic extrusions to pass through the alveolar cell junctions (Fig. 9A). In conjunction with this, the maximal immunofluorescence for the endothelial ICAM-1 occurred at the lamellar protrusion of PLC outlining EC at the segments of transmigration, as shown in XY projections (acquired with a 0.5-μm Z-step) presented in Figs. 9A and B. The 3-D arrangement of ICAM-1 and β_2-integrins was further analyzed using a stack of Z-optical sections of a PLCs entrapped in a fragment of microvessel (see an example of an optical section in Figs. 9C and D), to demonstrate spatial coordination of these CAMs in the "docking" construct. Z-Distribution of ICAM-1 in an axial Y-optical slice (0.5-μm step) of the stack of Z-optical sections revealed the presence of ICAM-1–enriched microvilli-like projections in the microvessels (Fig. 9F, green channel). Evidently, the assemblies of ICAM-1 clusters ensconced the PLC lamellipod, as shown in the image of the same diametric Y-optical slice in the presence of the projection of PLC β_2-integrins (Fig. 9E; ICAM-1, green channel; β_2-integrins, red channel). The estimated interaction of signals in red and green channels in this ROI was $r = 0.91$ (Pearson correlation). The ICAM-1–enriched assemblies occurred during the first 3 h after injury, persisted during the 24-h observation period, and apparently provided for the homing of the blood-borne cells essential for the tissue recovery and angiogenesis [*e.g.*, CD11b and the CD133 endothelial progenitor cells (Fig. 9G)] at the late period.

Chemotaxis of PLCs in lung injury has emerged as a hallmark of the acute respiratory distress syndrome. Activation of PLCs triggers the intraluminal release of enzymes from their cytoplasm vesicles and thus promotes microvascular inflammation. To assess these effects in the defined "inflammatomes," we then focused on MPO, a PLC marker, instead of β_2-integrins (see earlier). The 3-D arrangement of ICAM-1 and MPO was analyzed using a stack of Z-optical sections of a PLC in a fragment of microvessel as described earlier. The reconstructed image of projections of ICAM-1 and MPO is presented in Fig. 8A. Distribution of ICAM-1 and MPO in axial Y-optical slice (0.5-μm step) of the stack of Z-optical sections revealed their spatial colocalization in the vascular microvilli (Fig. 10B and C).

Interestingly, the MPO immunoreactivity could be observed at the ICAM-1 cluster assemblies even in the absence

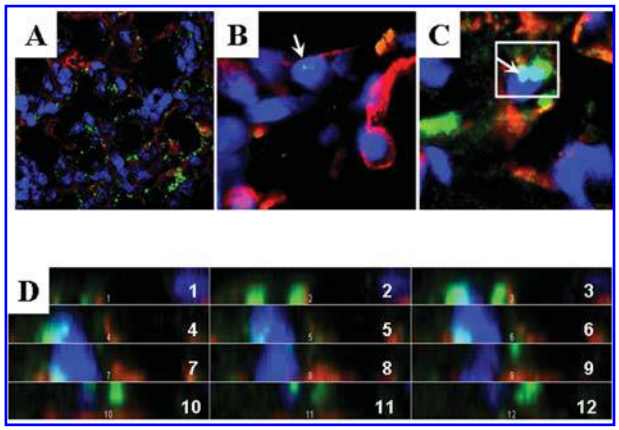

FIG. 7. Assessment of nuclear localization of Nrf2 in lung specimens from the animals subjected to shock-wave exposure or $NTA_2Fe_3^{2+}$ treatment (3 h after treatment). (**A–C**) Representative projections of Nrf2 (green channel, Alexa 488) in the lung specimens obtained from sham-treated (**A**, 100x magnification) ("sham to iron administration" group), SW-exposed (**B**, 100x magnification, 4x zoom), and $NTA_2Fe_3^{2+}$ treated (**C**, 100x magnification, 4x zoom) animals. Counterstaining of nuclei was with Hoechst 33342. Nuclear localization of Nrf2 appears as turquoise foci from interference of green and blue colors (arrows in **B** and **C**). (**D**) A montage of images obtained by 0.5-μm Y-reslicing of the stack of 10 Z projections of the indicated area in (**B**), which demonstrates the nuclear localization of Nrf2 (turquoise).

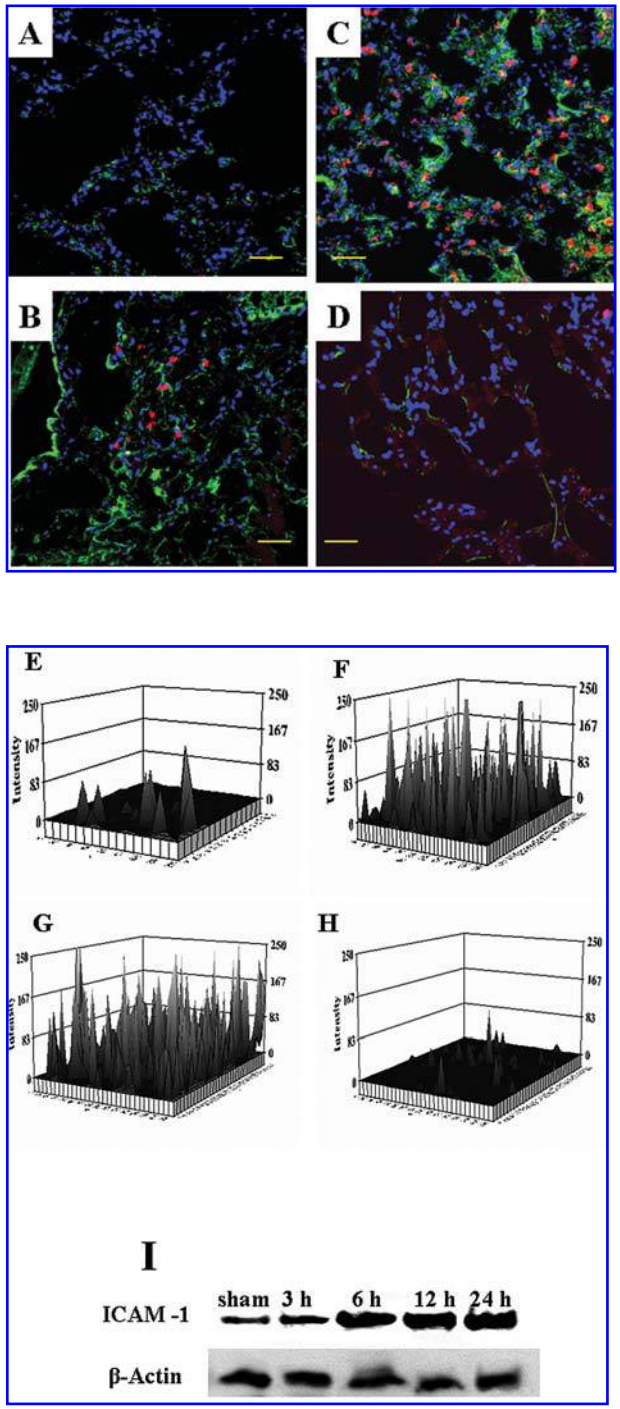

FIG. 8. Projections of the ICAM-1 adhesion molecules (green channel) and α_M-integrins, markers of the phagocytic leukocytes (red channel), in the lung specimens from the animals subjected to shock-wave exposure or $NTA_2Fe_3^{2+}$ treatment. (**A**) Sham treatment (sham to $NTA_2Fe_3^{2+}$ administration); (**B**) is 3 h after exposure to SW; (**C**) is 3 h after $NTA_2Fe_3^{2+}$ treatment. (**D**) is the same as (**C**), except $NTA_2Fe_3^{2+}$ was combined with HBED. The relative immunofluorescence of ICAM-1 in the specimens is presented in (**E–H**). (**F**) Immunoblot analysis of ICAM-1 protein in injured sections of lung subjected to SW exposure.

of chemotactic PLC. Because PLC is presumed to be the source of MPO, we considered the appearance of vascular immunoreactivity to MPO as evidence of the molecular footprint of previously adherent PLCs.

DISCUSSION

TEM is a central function of different types of the blood-borne cells and plays a key role in diverse biologic processes such as inflammation, wound healing, and tissue regeneration. Although the mechanisms underlying sequestration and TEM of the inflammatory PLCs have been extensively studied recently in different *in vitro* and *in vivo* models, these multistep events as well as their inflammatory consequences remain poorly understood in the pulmonary microvasculature after lung trauma. In particular, it is not known how iron released from the injured cells might participate in the signaling cascades during the PLC diapedesis. In the present study, we showed that lung trauma led to the increase in the ferric iron complexes, OS, and redox signaling in the lung parenchyma cells. To demonstrate a potential role of catalytically active iron in these events, we compared the effects of SW ex-

posure with those induced by administration of iron complexes. In these two models, we found similar patterns in CAM regulations during TEM. That encouraged us to pursue these effects further by examining some intercellular redox signaling pathways that control CAM expression.

The compensatory cell redox response to OS involves metabolic alterations at transcriptional and post-transcriptional levels. A number of regulators of these alterations (NF-κB, Nrf2, TRX, Ref-1, etc.) mediate redox signaling and therefore could be useful for assessment of the cell response to OS.

NF-κB is the first transcriptional factor shown to respond directly to OS. Activation of NF-κB has been shown recently to be a key redox-sensitive event associated with vascular dysfunction (8, 19, 36). In the EC cells, NF-κB is a prime target for OS, and its oxidation and nuclear translocation is associated with proinflammatory responses. The nuclear reduction of NF-κB by Ref-1 has been demonstrated recently to be essential for the NF-κB–dependent transcriptional expression of the EC ICAM-1 (15, 17, 22). In this study, we demonstrated the presence of redox-dependent induction of the nuclear translocation of NF-κB that was accompanied by an increase in the nuclear interaction of Ref-1/NF-κB in the injured lung. Based on the recent data and the current results, we assumed that these early responses of redox-sensitive factors could upregulate proinflammatory ICAM-1 while barrier functions of adhesion junctions were downregulated, as was previously documented in different models of oxidative damage (11, 36). The resulting alteration in the microvascular barrier function could explain the increase in the PLC transmigration in both models of lung injury. This assumption is based on several lines of evidence presented in this report and in recently published reports (11, 18, 21, 22, 30). Oxidative

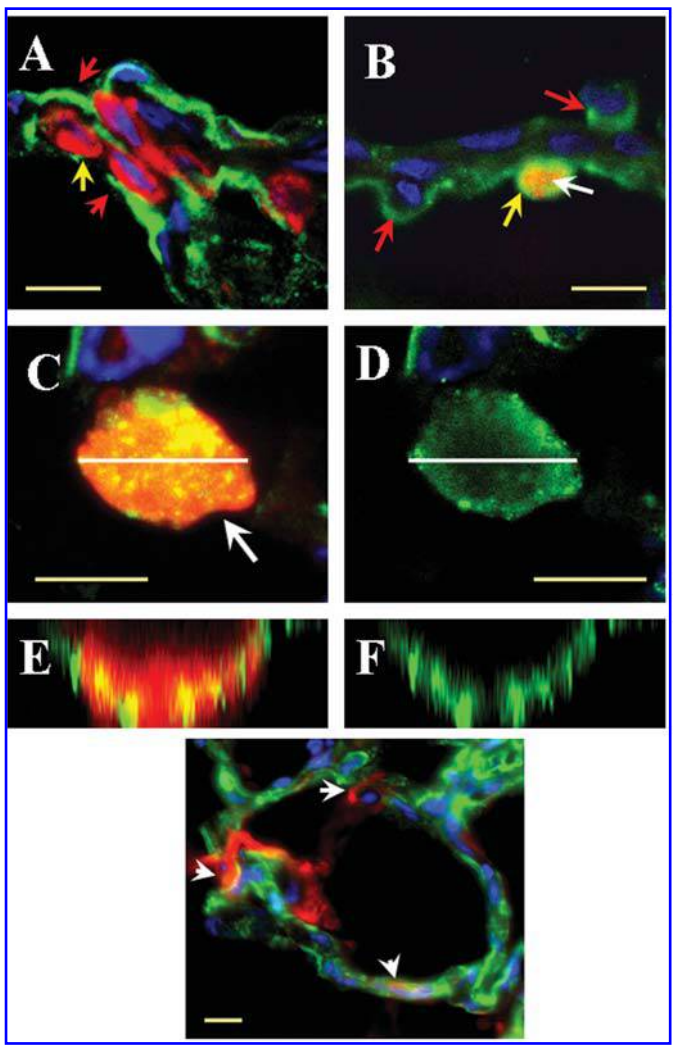

FIG. 9. Assessment of 3-D coordination of the ICAM-1 adhesion molecules (green channel) during trafficking of the phagocytic leukocytes (PLCs) (red channel) in the alveolar microvessels in the lung at 3 h after SW exposure. (**A**) Projections of transmigration of PLC lamellipod (yellow arrow) through vascular endothelium at site of ICAM-1–enriched microvilli-like formations (red arrow) in the lung microvessels. Immunofluorescence stainings were green (Alexa 488) for ICAM-1, red (Alexa 594) for the α_M-integrins, PLC markers, and blue (Hoechst 33342) for counterstaining. This image represents axial confocal sections (1-μm Z-step) of microvascular segments entrapped PLCs. Magnification is 100x with zoom 4x (bar, 10 μm). (**B**) Same as (**A**) except an image of axial confocal optical sections (1-μm Z-step) of microvessels (red arrows) in alveolar wall was taken to demonstrate interaction of the activated endothelium with a chemotactic PLC. Leading lamellipod of PLC moving along microvessel (red channel, α_M-integrins labeled with Alexa 594), and ICAM-1 enriched microvilli-like formations are indicated with white and yellow arrows. Magnification is 100x with zoom 4x (bar, 10 μm). (**C**) Overlay of the projections of the ED ICAM-1 (green channel, Alexa 488) and the PLC β_2-integrins (red channel, Alexa 594) in diametric confocal section (1-μm Z-step) of a microvascular-entrapped migrating PLC (white arrow). Magnification is 100x with zoom 10x (bar, 5 μm). (**D**) Projection of the **EC** ICAM-1 (green channel, Alexa 488) in the section of microvessel obtained by elimination of the projection of the PLC β_2-integrins (red channel, Alexa 594) in the image presented in **(C).** Magnification is 100x with zoom 10x (bar, 10 μm). (**E**) An image of the axial optical section of the microvessel with the entrapped PLC presented in (**C**) (at the point indicated with white line) and obtained by 0.5-μm Y-computer reslicing of the stack of 10 XY confocal images. Spatial colocalization of the PLC β_2-integrins (red channel, Alexa 594) and endothelial ICAM-1 (green, Alexa 488) adhesion molecules appears in orange-yellow because of interference of the green and red colors. (**F**) A reconstituted projection of the EC ICAM-1 (green channel, Alexa 488) in the axial optical section of a microvessel obtained by elimination of the projection of the PLC β_2-integrins (red channel, Alexa 594) in the image presented in (E). (G) Representative image of the infiltrated CD133 cells (red channel, Alexa 594) at the sites of expression of the endothelial ICAM-1 (green channel, Alexa 488) obtained from a lung specimen at 24 h after exposure to shock wave. Image was taken with magnification 40x and 2x zoom (bar, 10 μm). Infiltration of the CD 133 endothelial progenitor cells is indicated with white arrows.

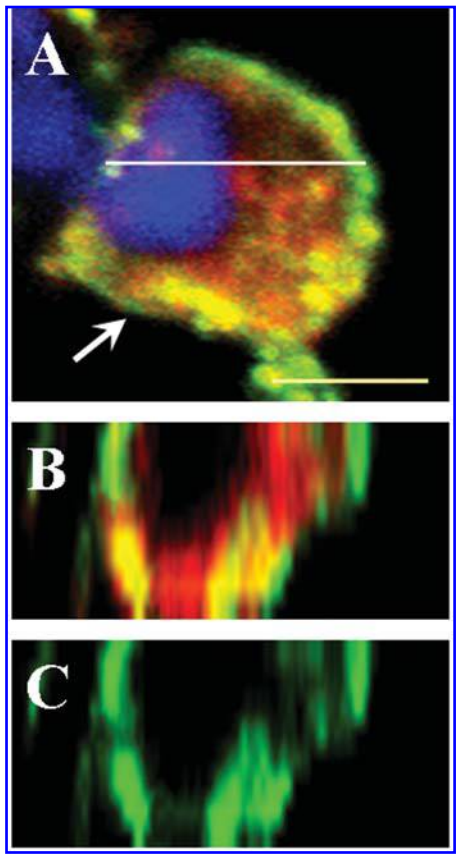

FIG. 10. Assessment of localization of myeloperoxidase (MPO) (red channel, Alexa 594) and endothelial ICAM-1 (green channel, Alexa 488) in the alveolar microvessel with an entrapped phagocytic leukocyte at 3 h after administration of $NTA_2Fe_3^{2+}$. (**A**) Image of Z-projections of MPO and ICAM-1 in a segment of alveolar microvessel (white arrow) entrapping a PLC. Magnification is 100x with zoom 10x (bar, 5 μm). (B) Image of the axial optical section of the microvessel with the entrapped PLC in (**A**) (at the point indicated with white line), and obtained by 0.5-μm Y-computer reslicing of the stack of 10 XY confocal images. Spatial colocalization of the PLC MPO (red channel, Alexa 594) and endothelial ICAM-1 (green, Alexa 488) adhesion molecules appears in orange-yellow because of interference of the green and red colors. (**C**) is a reconstituted projection of the EC ICAM-1 (green channel, Alexa 488) in the axial optical section of microvessel obtained by elimination of the projection of the PLC MPO (red channel, Alexa 594) in the image presented in (**B**).

stress is well accepted as a powerful and dynamic promoter of inflammation. Presumably, several direct and indirect effects of OS could result in the proinflammatory alterations. At present, the expression of several adhesion molecules, including VCAM-1 and ICAM-1, is widely accepted to be an OS-dependent process. Redox-dependent regulation of CAMs occurs at (a) the transcriptional level via redox-sensitive transcriptional factors (*e.g.*, NF-κB, Nrf2, Ref-1, AP-1), and (b) the post-transcriptional level via redox-sensitive MAP kinases (6, 8, 11, 19, 21, 30). Indirect effects could be mediated by proinflammatory chemokines, cytokines (*e.g.*, MIP-2, CINC-1, TNF-α), and histamine released in a redox-dependent manner in lung, which has been demonstrated previously in the current model of lung trauma and a variety of other models of the iron-associated lung inflammation (7, 12, 24).

The conducted assessment of the redox-sensitive factors provided evidence of the presence of the endothelial redox signaling at nuclear level at 3 h after treatments. However, the observed redox-dependent induction of ICAM-1 within that period was rather due to expression of constitutively present molecules than *de novo* produced protein that requires longer periods (see proposed mechanism in Fig. 11).

The correlation of increased lung iron and increased OS-induced signaling pathways seen in lung trauma suggested that local changes in lung iron may itself be part of the inflammatory signaling cascade. Our finding that similar changes could be induced by instillation of iron directly into the lung provides

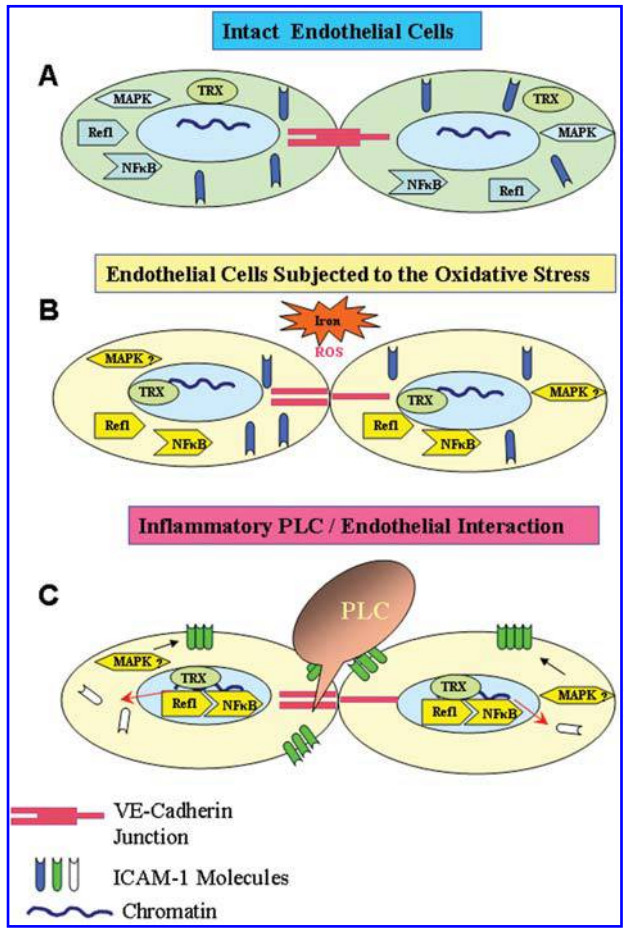

FIG. 11. Hypothetical scheme illustrating a sequence of events (A–C) associated with iron-dependent oxidative stress (B) and sustaining of ICAM-1 clusters in the lung microvessel: A proposed mechanisms for redox control of PLC "homing" by the inflammatory endothelium. The constitutively present unexpressed and expressed ICAM-1 molecules are shown in blue and green, respectively. Expression of the *de novo*–produced ICAM-1occurs at the late stages (>6 h) of inflammatory response.

support for this thesis, but one must be cautious in the conclusion that the effects are local. The lung is constantly being repopulated with infiltrated blood cells during the inflammatory process, including the progenitor stem cells released from bone marrow. In the present study, alveolar infiltration of individual CD133 cells (endothelial progenitor cells) occurred as early as 3 h after injury and was progressively increased at 24-h observation. They could likely use the same mechanisms as PLCs do in the vascular trafficking and TEM. From this perspective, the transcriptional expression of ICAM-1 at late stages of inflammation might be important to guide the blood-borne cells essential for remodeling and recovery of the injured tissue. Further studies of the iron-induced redox signaling and associated interplay of the cell-adhesion molecules during PLC diapedesis using cell co-cultures are warranted.

DISCLOSURE

The views, opinions, and/or findings contained herein are those of the authors and should not be construed as an official Department of the Army position, policy, or decision.

ACKNOWLEDGMENT

This work was supported by the Department of the Army Peer Reviewed Medical Research Program PR033201, by NIH HL 34360, HL 22559, and HL 33889 (to D.K.D.). We thank Sgt. Dara Wolfe, Ms. Sara Smith, and Dr. Vijayalakshmi Ayyagari for excellent technical assistance.

ABBREVIATIONS

BSA, bovine serum albumin; CAM, cell adhesion molecule; EC, endothelial cell; EPR, electron paramagnetic resonance; HBED, *N*,*N*′-bis (2-hydroxybenzyl) ethylenediamine-*N*,*N*′-diacetic acid; HbNO, adduct of nitric oxide with hemoglobin; ICAM-1, intercellular adhesion molecule 1; MPO, myeloperoxidase; NF-κB, nuclear factor κB; Nrf2, nuclear factor E2–related factor 2 (Keap1/Nrf2); $NTA_2Fe_3^{2+}$, iron (ferrous) nitriloacetate; O.C.T., optimal cutting temperature; 3NTyr, 3-nitrotyrosine; OS, oxidative stress; PBS, phosphate-buffered saline solution; PECAM-1, platelet/endothelial cell adhesion molecule-1; PLC, phagocytic leukocyte; Ref-1, redox factor-1; SW, shock wave; TEM, transendothelial migration (*i.e.*, diapedesis); TRX, thioredoxin 1; VCAM-1, vascular cell adhesion molecule 1; VE-cadherin, vascular endothelial cadherin-5 (CD144).

REFERENCES

1. Barreiro O, Yanez-Mo M, Serrador JM, Montoya MC, Vicente-Manzanares M, Tejrdor R, Furthmayr H, and Sanchez-Madrid F. Dynamic interaction of VCAM-1 and ICAM-1 with moesin and ezrin in a novel endothelial docking structure for adherent leukocytes. *J Cell Biol* 157: 1233–1245, 2002.
2. Beck-Schimmer B, Schimmer RC, Schmal H, Flory CM, Friedl HP, Pasch T, and Ward PA. Characterization of rat lung ICAM-1. *Inflamm Res* 47: 308–315, 1998.
3. Bergeron RJ, Wiegand J, and Brittenham GM. HBED: The continuing development of a potential alternative to deferoxamine for iron-chelating therapy. *Blood* 93: 370–375, 1999.
4. Carman CV and Springer TA. A transmigratory cup in leukocyte diapedesis both through individual vascular endothelial cells and between them. *J Cell Biol* 167:377–388, 2004.
5. Carman CV, Jun CD, Salas A, and Springer TA. Endothelial cells proactively form microvilli-like membrane projections upon intercellular adhesion molecules-1 engagement of leukocyte LFA-1. *J Immunol* 171: 6135–6144, 2003.
6. Chen XL, Zhang Q, Zhao R, Ding X, Tummala PE, and Medford RM. Rac1 and superoxide are required for the expression of cell adhesion molecules induced by tumor necrosis factor-alpha in endothelial cells. *FASEB J* 18: 1321–1323, 2004.
7. Chio AJ, Piantadosi CA, Wang X, Dailey LA, Stonehuerner JD, Madden MC, Yang F, Dolan KG, Garrick MD, and Garrick LM. Divalent metal transporter-1 decreases metal-related injury in the lung. *Am J Physiol Lung Cell Mol Physiol* 289: L460–L467, 2005.
8. Costanzo A, Moretti F, Burgio VL, Bravi C, Guido F, Levrero M, and Puri PL. Endothelial activation by angiotensin II through NFkappaB and p38 pathways: involvement of NFkappaB-inducible kinase (NIK), free oxygen radicals, and selective inhibition by aspirin. *J Cell Physiol* 195: 402–410, 2003.
9. Dick CA, Brown DM, Donaldson K, and Stone V. The role of free radicals in the toxic and inflammatory effects of four different ultrafine particle types. *Inhal Toxicol* 15: 39–52, 2003.
10. Doerschuk CM. Mechanisms of leukocyte sequestration in inflamed lungs. *Microcirculation* 8: 71–88, 2001.
11. Dress F, Pokutta S, Yamada S, Nelson WJ, and Weiss WI. Alpha-Catenin is a molecular switch that binds E-cadherin, and beta-catenin regulates actin-filament assembly. *Cell* 123: 903–915, 2005.
12. Gao X, Kouklis P, Xu N, Minshall RD, Sandoval R, Vogel SM, and Malik AB. Reversibility of increased microvessel permeability in response to VE-cadherin disassembly. *Am J Physiol Lung Cell Mol Physiol* 279: L1218–L1225, 2000.
13. Gorbunov NV, McFaul SJ, Januszkiewicz A, and Atkins JL. Pro-inflammatory alterations and status of blood plasma iron in a model of blast-induced lung trauma. *Int J Immunopathol Pharmacol* 18:547–556, 2005.
14. Gorbunov NV, Asher LV, Ayyagari V, and Atkins JL. Inflammatory leukocytes and iron turnover in experimental hemorrhagic lung trauma. *Exp Mol Pathol* 80:11–25, 2005.
15. Gorbunov NV, Das DK, Goswami SK, Gurusamy N , and Atkins JL. Nitric oxide (NO), redox signaling, and pulmonary inflammation in a model of polytrauma. In: *Proceeding of the XIII Congress of the Society for Free Radical Research International, Davos (Switzerland),* edited by MEDIMOND S.r.l, Bologna, Italy. 2006, pp. 139–144.
16. Hedley D, Pintilie M, Woo J, Nicklee T, Morrison A, Birle D, Fyles A, Milosevic M, and Hill R. Up-regulation of redox mediators thioredoxin and apurinic/apyrimidinic excision (APE/Ref-1) in hypoxic microregions of invasive cervical carcinomas, mapped using multispectral, wide-field fluorescence image analysis. *Am J Pathol* 164: 557–565, 2004.
17. Hirota K, Murata M, Sachi Y, Nakamura H, Takeuchi J, Mori K, Yodoi J. Distinct roles of thioredoxin in the cytoplasm and in the nucleus: a two-step mechanism of redox regulation of transcription factor NF-kappaB. *J Biol Chem* 274: 27891–27897, 1999.
18. Kabe Y, Ando K, Hirao S, Yoshida M, and Handa H. Redox regulation of NF-κB activation: distinct redox regulation between the cytoplasm and the nucleus. *Antioxid Redox Signal* 7: 395–402, 2005.
19. Kartikasari AE, Georgiou NA, Visseren FL, van Kats-Renaud H, Sweder van Asbeck B, and Marx JJ. Endothelial activation and induction of monocyte adhesion by nontransferrin-bound iron present in human sera. *FASEB J* 20:353–355, 2006.
20. Kuldo JM, Westra J, Asgeirsdottir SA, Kok RJ, Oosterhuis K, Rots MG, Schouten JP, Limburg PC, and Molema G. Differential effects of NF-(kappa)B and p38 MAPK inhibitors and combinations thereof on TNF-(alpha)- and IL-1(beta)-induced proinflammatory status of endothelial cells in vitro. *Am J Physiol Cell Physiol* 289: C1229–C1239, 2005.

21. Lau D, Mollnau H, Eiserich JP, Freeman BA, Daiber A, Gehling, UM, Brummer J, Rudolph V, Munzel T, Heitzer T, Meinertz T, and Baldus S. Myeloperoxidase mediates neutrophil activation by association with CD11b/CD18 integrins. *Proc Natl Acad Sci U S A* 102: 431–436, 2005.
22. Lum H and Roebuck KA. Oxidant stress and endothelial cell dysfunction. *Am J Physiol Cell Physiol* 280: C719–C741, 2001.
23. Nakamura T, Nakamura H, Hoshino T, Ueda S, Wada H, and Yodoi J. Redox regulation of lung inflammation by thioredoxin. *Antioxid Redox Signal* 7: 60–71, 2005.
24. Nguyen T, Yang CS, Pickett CB. The pathways and molecular mechanisms regulating Nrf2 activation in response to chemical stress. *Free Radic Biol Med* 37: 433–441, 2004.
25. Nishi T, Shimizu N, Hiramoto M, Sato I, Yamaguchi Y, Hasegawa M, Aizawa S, Tanaka H, Kataoka K, Watanabe H, Handa H. Spatial redox regulation of a critical cysteine residue of NF-kappa B *in vivo*. *J Biol Chem* 277: 44548–445456, 2002.
26. Roberts ES, Richards JH, Jaskot R, and Dreher KL. Oxidative stress mediates air pollution particle-induced acute lung injury and molecular pathology. *Inhal Toxicol* 15: 1327–1346, 2003.
27. Ronald JA, Ionescu CV, Rogers KA, and Sanding M. Differential regulation of transendothelial migration of THP-1 cells by ICAM-1/LFA-1 and VCAN-1/VLA-4. *J Leukoc Biol* 70: 601–609, 2001.
28. Samuni AM, Afeworki M, Stein W, Yordanov AT, DeGraff W, Krishna MC, Mitchell JB, and Brechbiel MW. Multifunctional antioxidant activity of HBED iron chelator. *Free Radic Biol Med* 30: 170–177, 2001.
29. Sato N, Suzuki Y, Nishio K, Suzuki K, Naoki K, Takeshita K, Kudo H, Miyao N, Tsimura H, Serizawa H, Suematsu M, and Yamaguchi K. Role of ICAM-1 for abnormal leukocyte recruitment in the microcirculation of bleomycin-induced fibrotic lung injury. *Am J Respir Crit Crit Care Med* 161: 1681–1688, 2000.
30. Springer TA. Traffic signals for lymphocyte recirculation and leukocyte emigration: the multistep paradigm. *Cell* 76: 301–314, 1994.
31. Springer TA and Wang JH. The three-dimensional structure of integrins and their ligands, and conformational regulation of cell adhesion. *Adv Protein Chem* 68: 29–63, 2004.
32. True AL, Rahman A, and Malik AB. Activation of NF-kappaB induced by H(2)O(2) and TNF-alpha and its effects on ICAM-1 expression in endothelial cells. *Am J Physiol Lung Cell Mol Physiol* 279: L302–L311, 2000.
33. Wagner JG and Roth RA. Neutrophil migration mechanisms, with an emphasis on the pulmonary vasculature. *Pharmacol Rev* 52: 349–374, 2000.
34. Wang Q, Pfeiffer GR, Stevens T, and Doerschuk CM. Lung microvascular and arterial endothelial cells differ in their responses to intercellular adhesion molecule-1 ligation. *Am J Respir Critic Care Med* 166: 872–877, 2002.
35. Ward PA, Mulligan MS, Vaporciyan AA, and Eppinger MJ. Adhesion molecules in experimental lung inflammatory injury. In: Ward PA, Fantone JC, eds. *Adhesion molecules and the lung.* Marcel Dekker, New York, 1996, pp. 150–176.
36. Wawryk SO, Novotny JR, Wicks IP, Wilkinson D, Maher D, Salvaris E, Welch K, Fecondo J, and Boyd AW. The role of the LFA-1/ICAM-1 interaction in human leukocyte homing and adhesion. *Immunol Rev* 108:135–161, 1989.
37. Wei SJ, Botero A, Hirota K, Bradbury CM, Markovina S, Laszlo A, Spitz DR, Goswami PC, Yodoi J, and Gius D. Thioredoxin nuclear translocation and interaction with redox factor-1 activates the activator protein-1 transcription factor in response to ionizing radiation. *Cancer Res* 60: 6688–6695, 2000.
38. Zhao X, Alexander JS, Zhang S, Zhu Y, Sieber NJ, Aw TY, and Carden DL. Redox regulation of endothelial barrier integrity. *Am J Physiol Lung Cell Mol Physiol* 281: L879–L886, 2001.
39. Zouki C, Zhang SL, Cjan JS, and Filep JG. Peroxynitrite induces integrin-dependent adhesion of human neutrophils to endothelial cells via activation of the Raf-1/MEK/Erk pathway. *FASEB J* 15: 25–27, 2001.

Address reprint requests to:
Dr. Nikolai V. Gorbunov
WRAIR/MCR
503 Robert Grant Avenue, 1A14
Silver Spring, MD, 20910–7500

E-mail: nikolai.gorbounov@na.amedd.army.mil

Date of first submission to ARS Central, April 24, 2006; date of acceptance, October 17, 2006.

This article has been cited by:

1. Nikolai V. Gorbunov, James L. Atkins, Narasimman Gurusamy, Bruce R. Pitt. 2011. Iron-induced remodeling in cultured rat pulmonary artery endothelial cells. *BioMetals* . [CrossRef]
2. Nikolai V. Gorbunov, Juliann G. Kiang. 2009. Up-regulation of autophagy in small intestine Paneth cells in response to total-body #-irradiation. *The Journal of Pathology* **219**:2, 242-252. [CrossRef]
3. Arshad Rahman , Fabeha Fazal . 2009. Hug Tightly and Say Goodbye: Role of Endothelial ICAM-1 in Leukocyte Transmigration. *Antioxidants & Redox Signaling* **11**:4, 823-839. [Abstract] [Full Text PDF] [Full Text PDF with Links]
4. Sandra E. Gomez-Mejiba, Zili Zhai, Hammad Akram, Quentin N. Pye, Kenneth Hensley, Biji T. Kurien, R. Hal Scofield, Dario C. Ramirez. 2009. Inhalation of environmental stressors & chronic inflammation: Autoimmunity and neurodegeneration. *Mutation Research/Genetic Toxicology and Environmental Mutagenesis* **674**:1-2, 62-72. [CrossRef]
5. Sun Yang , Frank L. Meyskens . 2009. Apurinic/Apyrimidinic Endonuclease/Redox Effector Factor-1(APE/Ref-1): A Unique Target for the Prevention and Treatment of Human Melanoma. *Antioxidants & Redox Signaling* **11**:3, 639-650. [Abstract] [Full Text HTML] [Full Text PDF] [Full Text PDF with Links]
6. Savita Khanna , Han-A Park , Chandan K. Sen , Trimurtulu Golakoti , Krishanu Sengupta , Somepalli Venkateswarlu , Sashwati Roy . 2009. Neuroprotective and Antiinflammatory Properties of a Novel Demethylated Curcuminoid. *Antioxidants & Redox Signaling* **11**:3, 449-468. [Abstract] [Full Text HTML] [Full Text PDF] [Full Text PDF with Links]
7. Kishor K. Bhakat , Anil K. Mantha , Sankar Mitra . 2009. Transcriptional Regulatory Functions of Mammalian AP-Endonuclease (APE1/Ref-1), an Essential Multifunctional Protein. *Antioxidants & Redox Signaling* **11**:3, 621-637. [Abstract] [Full Text HTML] [Full Text PDF] [Full Text PDF with Links]
8. SUN YANG, Frank L Meyskens. 2008. Apurinic/apyrimidinic endonuclease /redox effector factor-1(APE/Ref-1) a unique target for the prevention and treatment of human melanoma. *Antioxidants & Redox Signaling* **0**:ja, 080820101352867. [CrossRef]
9. Nikolaos A Maniatis, Stylianos E Orfanos. 2008. The endothelium in acute lung injury/acute respiratory distress syndrome. *Current Opinion in Critical Care* **14**:1, 22-30. [CrossRef]